# Mapping Photothermally Induced Gene Expression in Living Cells and Tissues by Nanorod-Locked Nucleic Acid Complexes

Reza Riahi,[†] Shue Wang,[†] Min Long,[‡,§] Na Li,[⊥] Pei-Yu Chiou,[‖] Donna D. Zhang,[‡] and Pak Kin Wong[†,*]

[†]Department of Aerospace and Mechanical Engineering, University of Arizona, Tucson, Arizona 85721, United States, [‡]Department of Pharmacology and Toxicology, University of Arizona, Tucson, Arizona 85724, United States, [§]Department of Endocrinology, Xinqiao Hospital, Third Military Medical University, Chongqing 400037, People's Republic of China, [⊥]Department of Mechanical and Aerospace Engineering, University of Miami, Coral Gables, Florida 33146, Unites States, and [‖]Department of Mechanical and Aerospace Engineering, University of California, Los Angeles, California 90095, United States

ABSTRACT The photothermal effect of plasmonic nanostructures has numerous applications, such as cancer therapy, photonic gene circuit, large cargo delivery, and nanostructure-enhanced laser tweezers. The photothermal operation can also induce unwanted physical and biochemical effects, which potentially alter the cell behaviors. However, there is a lack of techniques for characterizing the dynamic cell responses near the site of photothermal operation with high spatiotemporal resolution. In this work, we show that the incorporation of locked nucleic acid probes with gold nanorods allows photothermal manipulation and real-time monitoring of

gene expression near the area of irradiation in living cells and animal tissues. The multimodal gold nanorod serves as an endocytic delivery reagent to transport the probes into the cells, a fluorescence quencher and a binding competitor to detect intracellular mRNA, and a plasmonic photothermal transducer to induce cell ablation. We demonstrate the ability of the gold nanorod-locked nucleic acid complex for detecting the spatiotemporal gene expression in viable cells and tissues and inducing photothermal ablation of single cells. Using the gold nanorod-locked nucleic acid complex, we systematically characterize the dynamic cellular heat shock responses near the site of photothermal operation. The gold nanorod-locked nucleic acid complex enables mapping of intracellular gene expressions and analyzes the photothermal effects of nanostructures toward various biomedical applications.
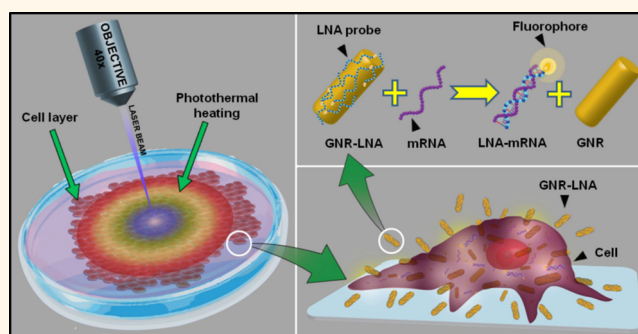
KEYWORDS: gold nanorods · locked nucleic acids · plasmonic nanostructures · photothermal effects · heat shock response · intracellular detection

The advent of plasmonic nanostructures has opened new opportunities in fundamental biology and translational medicine.[1−11] Photothermal therapy of cancer and other diseases, for instance, is based on plasmonic nanoparticle-enhanced laser absorption to treat the target cells or tissues.[4] With the leaky vasculature of tumor tissues or by specific surface functionalization, plasmonic nanoparticles can preferentially accumulate in cancer cells.[12−14] The high concentration of nanoparticles in the cancer tissue enables photothermal operation, such as localized heating and cell ablation, using near-infrared laser, which has a

large penetration depth in tissue. Photothermal therapy of cancer, for instance, utilizes the plasmonic effect of gold nanorods with near-infrared laser.[4,15] Furthermore, plasmonic nanostructures coupled with small interfering RNA (siRNA) have been applied to control photonic gene circuits.[7,16] The siRNA—nanostructure technique allows optically addressable release of siRNA and provides an effective approach for precise perturbation of gene circuits without permanent genomic medications. A photothermal nanoblade has also been developed for large cargo delivery in living cells.[17] The technique utilizes a glass microcapillary pipet with a thin metal

film sputtered onto the tip. To transfer cargo into living cells, the tip is positioned to lightly touch the membrane of a cell and a short laser pulse, which causes the formation of a nanoscale cavitation bubble due to laser−metal structure coupling at the tip to locally disrupt the contacting lipid bilayer. In addition, dielectrophoretic force can also be induced for cell manipulation by focusing a polarized laser to a gold nanoshell array or other nanostructures.[8,10] The laser excites localized surface plasmon resonance and creates high nonuniform electric field for dielectrophoretic manipulation.

In most biological and clinical applications, short laser pulses or low laser powers are applied to avoid unnecessary harmful effects to cells and tissues. With the increasing applications of plasmonic nanostructures, unwanted effects could be introduced to cells in or near the site of photothermal operation, especially in situations that require long excitation duration or high laser power.[18] In particular, localized heating could induce cellular stress responses, such as heat shock proteins (HSPs), which are molecular components in the cellular defense mechanism against environmental insults. For photothermal therapy, the upregulation of heat shock protein may enhance tumor cell imparting resistance to chemotherapy and potentially increases tumor recurrence induced by heat stress.[19−22] Furthermore, excessive heating to the neighboring regions could damage the healthy tissues. Despite its importance, little is known about the spatiotemporal gene expression distribution for viable cells and tissues near the region of photothermal operation.

In this study, we incorporate locked nucleic acid (LNA) probes with gold nanorods (GNRs) for monitoring the spatiotemporal gene expression near the site of photothermal operation. LNA probes for detecting intracellular mRNAs are designed and characterized in viable human cells and mice tissues. The effects of laser power and duration on the spatiotemporal temperature distribution are measured and correlated with the gene expression profiles measured by the GNR−LNA complexes. Computational analysis is also performed to elucidate the heat transfer characteristics and optimize the irradiation conditions for single-cell photothermal ablation. Furthermore, the dynamic cellular heat shock responses under different conditions are characterized systematically near the site of photothermal operation.

RESULTS AND DISCUSSION

Figure 1a illustrates the design of the GNR−LNA complex for mapping photothermally induced gene expression in living cells and tissues. Detection of intracellular mRNA in individual cells is achieved by taking advantage of the gold nanoparticles' intrinsic quenching property[23−27] and the gold nanoparticle− nucleic acid binding affinity.[28] In this approach,

5′ fluorescently labeled LNA probes with alternating LNA/DNA monomers are attached to GNRs, spontaneously forming GNR−LNA complexes. Alternating LNA/DNA monomers were previously shown to improve the probe stability for intracellular detection and adjust the binding affinity.[29−32] In the absence of a target mRNA, the fluorophore conjugated to the LNA probe is quenched due to proximity with the GNR. With the specific target, the LNA probe is displaced from the GNR thermodynamically and hybridizes to the mRNA, allowing the fluorophore to fluoresce.

We characterized the GNR−LNA complexes for intracellular detection in human breast adenocarcinoma cells and mice tissues. Figure 1b shows the intensity of LNA probes targeting β-actin and heat shock protein 70 (HSP70) in the alveolar structures of mice lung tissues. High intensities were observed for the probes. In contrast, the random probe had a low intensity throughout the experiment. Similar results were observed in MCF7 cells and mice liver tissues (Supporting Information Figure S1). Furthermore, the GNR effectively quenched the fluorophore and displayed a quenching efficiency 2.4 times higher than an organic quencher conjugated to a complementary LNA/DNA sequence (Figure S2a,b). The specificity of the assay was tested by the random probe control (Figure S2c). Without a target, both probes exhibited a low background level comparable to the buffer solution. The β-actin target significantly increased the intensity of the β-actin probe but not the random probe, demonstrating the specificity of the assay. To examine the effect of laser irradiation, laser was irradiated to the GNR−LNA solution and did not show any observable effect (Figure S2d). These results collectively support the effectiveness of the GNR−LNA complex for gene expression analysis.

With GNRs, individual cells in tissues and monolayer cultures could also be selectively ablated by focusing the laser to the cell (Figure 1c and movie S1). Control experiments without GNRs were also performed (movie S2). We utilized UV−vis−NIR spectrophotometry to measure the absorption spectrum of the GNR for optimizing the photothermal effect (Figure S3a). The length and width of the GNR were 67 and 10 nm, and there were two peaks at 900 and 570 nm corresponding to the longitudinal and transverse surface plasmon resonance modes.[33] Dark-field images illustrated that the uptake of GNRs was uniform among the cells (Figure 2a,b and Figure S3b). To determine the amount of GNRs in the cell, we performed inductively coupled plasma mass spectrometry measurement after 12 h of incubation (Figure S3c). The amount of intracellular GNR could be controlled by adjusting the concentration of GNR during incubation. With an appropriate concentration (e.g., 4000 GNRs/cell), the GNRs displayed minimal cell toxicity, as indicated by cell morphology and viability, and provided an optimum photothermal effect
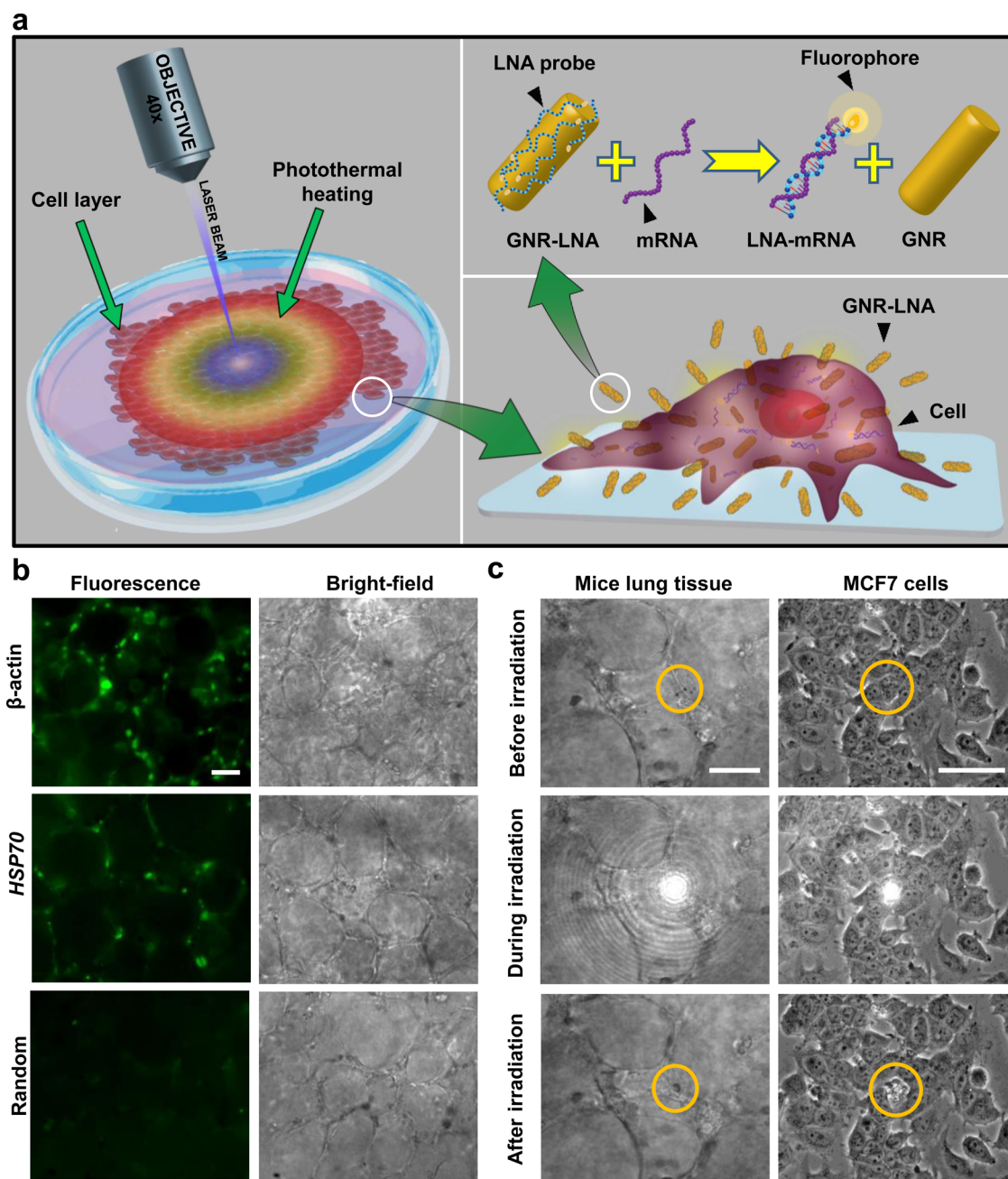
Figure 1. Multimodal GNR–LNA complexes for intracellular gene expression mapping and photothermal operation. (a) Schematic of the photothermal experiment. To induce photothermal effects, the laser was focused to a cell of interest. The laser energy is coupled by the plasmonic GNRs in the cells. The GNR also delivers the LNA probes into the cells and quenches the fluorophore conjugated to the probe. With a target mRNA, the probe displaces from the GNR and hybridizes to the target, allowing intracellular gene expression analysis in living cells and tissues. (b) Intracellular gene expression of β-actin and *HSP70* mRNAs in mice lung tissues. A random sequence is designed as the negative control. The fluorescence intensity in the cytoplasm of each cell can be extracted from the images to map the spatiotemporal gene expression dynamics. Scale bar, 50 μm. (c) Photothermal ablation experiment performed by focusing the laser to a target cell of interest in mice lung tissues (left) and monolayer cultures (right). Cycles indicate the target cell in the ablation experiments. Scale bars, 50 μm. Data are representative images from three independent experiments.

(Figure S3d,e).[34–37] This concentration was thus used throughout this study.

The photothermal temperature elevation at this GNR concentration was then characterized using miniaturized thermocouples (10 μm diameter) and an infrared camera. With continuous irradiation to a target cell (150 mW; 15 μm beam size) for 1 min, a temperature gradient was established and cells nearby experienced different temperatures depending on their positions (Figure 2c,d). The temperature rise at the irradiation site could be controlled from 2 to 15 °C by adjusting the laser power (Figure 2e). Without GNRs, the temperature was only modulated slightly (<2 °C), and the cells did not show any observable effect (Figure S3f,g).
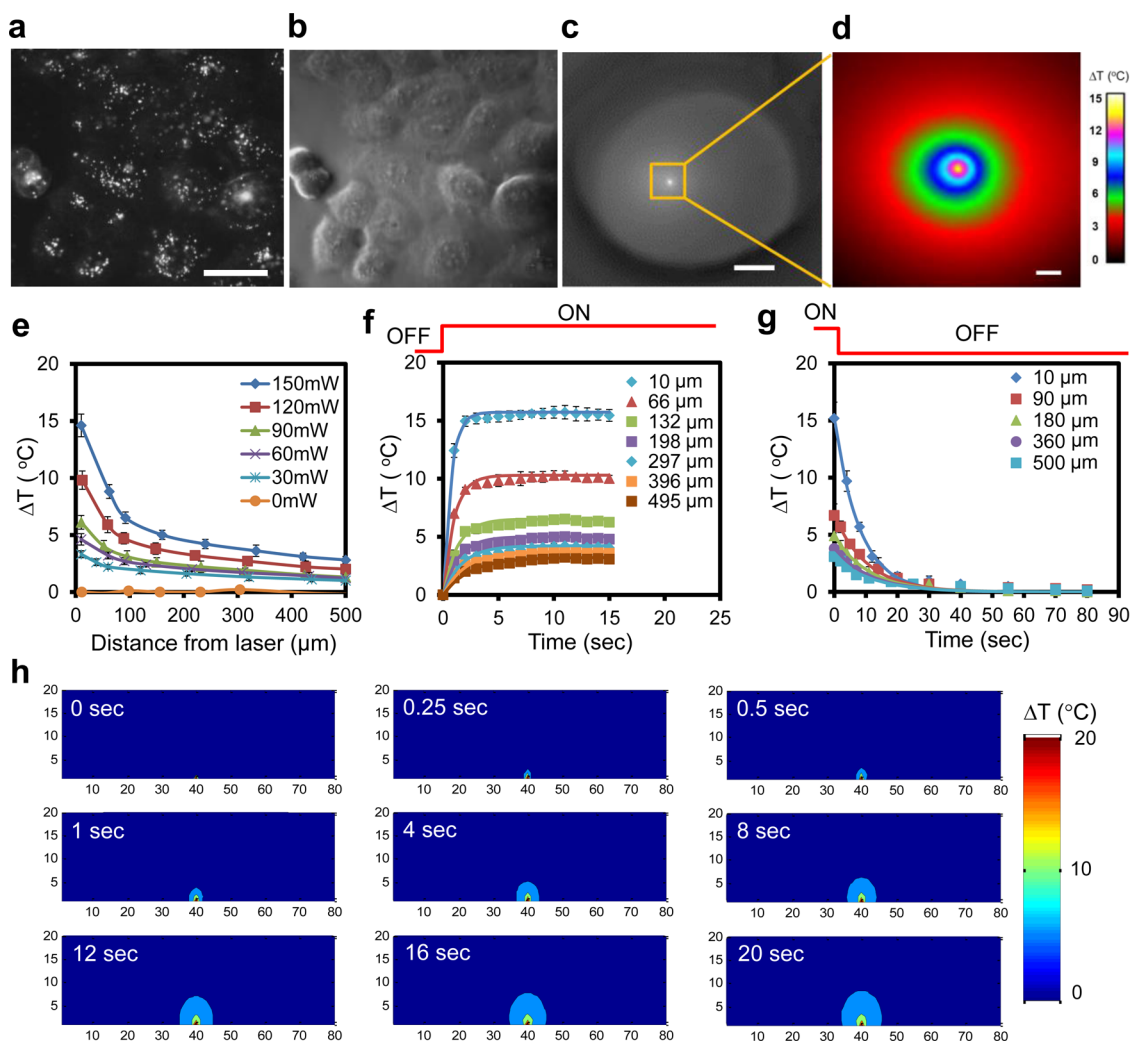
Figure 2. Characteristics of GNR for photothermal operation. (a,b) Dark-field and bright-field images for characterizing cellular uptake of GNRs. The cells were incubated with 2×10^{11} GNR/mL for 12 h. Scale bar, 25 μm. (c) Infrared thermometry for measuring the temperature profile in a glass bottom tissue culture dish. A single cell is irradiated by the laser to induce localized photothermal heating. Scale bar, 1 mm. (d) Temperature distribution near the laser. Scale bar, 150 μm. Color bar indicates the temperature elevation with respect to the reference temperature (37 °C). (e) Temperature distributions near the laser with different values of laser power after 1 min irradiation. Laser was focused at the origin. (f) Heating experiments measured by miniaturized thermocouples with laser irradiation at 150 mW. Data were fitted with exponential functions to extract the heating time constants. (g) Thermal cooling experiments monitored by miniaturized thermocouples. Data were fitted with exponential functions to extract the cooling time constants. (h) Computational simulation illustrating the evolution of the spatial temperature profiles with continuous laser irradiation. The simulation domain consists of 1600 elements, and each element represents 100 μm by 100 μm. The size of the domain is 2 mm by 8 mm. Color bar indicates the amplitude of temperature elevation.

To determine the heat transfer characteristics, we performed thermal cooling and heating experiments. The heating time constants were between 1 and 4 s depending on the distance from the laser (Figure 2f). A longer constant in the range of 15−25 s was observed for cooling (Figure 2g). To elucidate the heat transfer process, a numerical simulation was also performed (Figure 2h and Figures S4−S7). Effects of laser duration on the temperature profile are described in supplementary section B and movies S3−S6. The results were in good agreement with the experiments and revealed that the thermal time constants are related to the convective heat transfer at the boundary and the heat accumulation of the bulk solution.

To examine the spatial cellular heat shock responses, the intensity distributions of the *HSP70* probes were measured in human cells and mice lung tissues (Figure S8 and Figure 3). The laser beam size was focused to smaller than a cell (∼15 μm) with an optical intensity of 0.85 mW/μm². The *HSP70* expressions were examined before and after laser irradiation in lung tissues (Figure 3a,b). The spatial gene expression profiles were dependent upon the irradiation duration. For 5 min irradiation, the gene expression in neighboring cells near the irradiation area was upregulated and displayed a gradient in response (Figure 3c. With longer irradiation (*e.g.*, 15 or 30 min), the cell response was upregulated in 100−300 μm away from the laser and
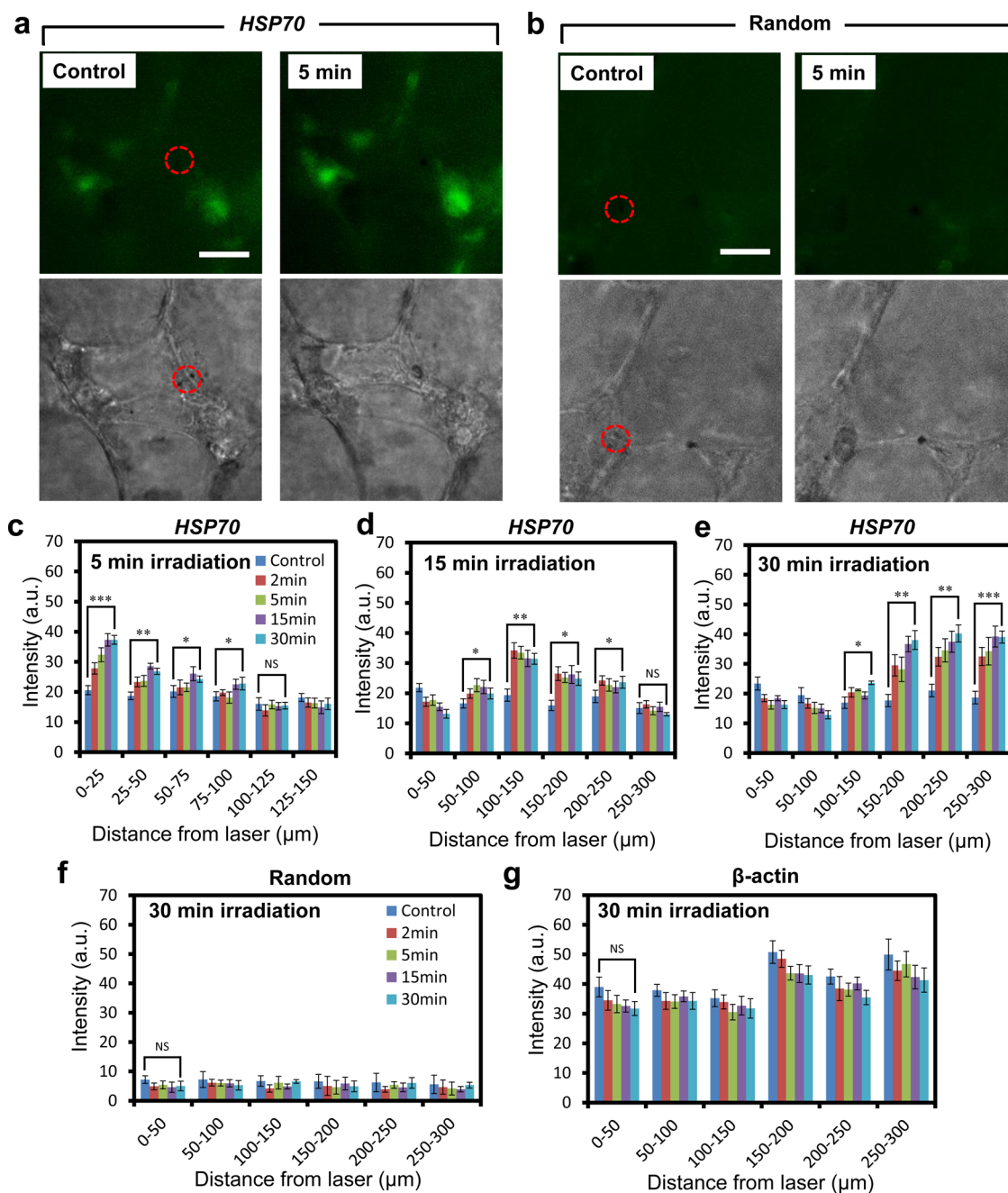
Figure 3. Mapping of *HSP70* gene expression distributions induced by laser irradiation of single cells. (a,b) Fluorescence and bright-field images before and after 5 min of laser irradiation. The LNA probes target *HSP70* mRNA and a random sequence. Red circles indicate the locations of laser irradiation in lung tissues. Scale bar, 25 μm. (c−e) Intercellular gene expression distribution in different locations. Laser was focused at the origin. Intensity was measured before and at 2, 5, 15, and 30 min after laser irradiation. The experiment was repeated with 5, 15, and 30 min of laser irradiation. A single cell was irradiated in each experiment. (f,g) Laser irradiation experiments were performed using the random and β-actin probes with 30 min irradiation. All other conditions were the same as the *HSP70* experiments. Statistical analysis, *n* = 3 (NS, not significant; *$P < 0.05$; **$P < 0.01$; ***$P < 0.001$).

was downregulated in the vicinity of the laser (Figure 3d,e). To confirm that the observed gene expression response is not a result of thermal dissociation of the GNR−LNA complexes, the random and β-actin probes were used as control, showing uniform intensities throughout the experiment (Figure 3f,g). The intensities were primarily compared between different time points at the same location due to the random distribution of the initial intensity. This observation confirmed that the temperature elevation induced at different distance from the heat source did not induce nonspecific release of the probes from the GNRs inside the cells. The general trend of the spatiotemporal gene expression responses was similar in MCF7 cell cultures, despite the differences in architectures, heat transfer characteristics, and cell types (Figure S8).
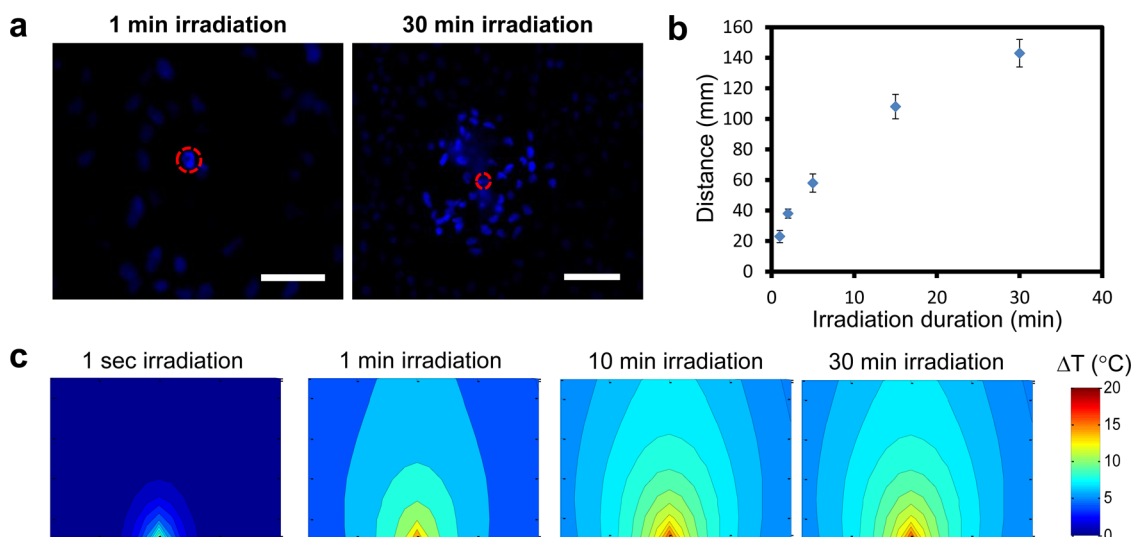
Figure 4. (a) Cell apoptosis measurement using Hoechst 33342. The distributions of apoptotic cells after 1 and 30 min of laser irradiation. Scale bars, 50 μm (left) and 100 μm (right). (b) Region of cell death as a function of the duration of laser irradiation. (c) Computational simulation showing the temperature distribution for different durations of laser irradiation. The domain of the simulation was 2 mm by 8 mm. Only the temperature near the laser (2 mm by 2 mm) is shown to illustrate the local temperature distribution. Color bar indicates the amplitude of temperature elevation.

To investigate the reduction of *HSP70* expression near the laser at long irradiation, the cells were evaluated with a fluorescent apoptosis assay. Figure 4a shows the distribution of apoptotic cells relative to the location of laser irradiation. With a short duration (*e.g.*, 1 min or less), cell ablation was achieved at the single-cell level (~25 μm). Increasing the duration expanded the region of apoptotic cells (Figure 4b), which correlated to the area of *HSP70* reduction. For instance, 30 min of irradiation induced cell apoptosis in a region ~140 μm from the laser. The *HSP70* reduction and cell apoptosis near the site of photothermal operation were determined by the coupled effects of spatial temperature profile and the duration that cells experienced the elevated temperature. With continuous irradiation, heat accumulation was observed in the bulk solution, which extended the high-temperature region (Figure 4c). The elevated temperature reduced *HSP70* expression and induced cell apoptosis. Collectively, these results revealed the effects of irradiation duration on the cellular heat shock stress response and determined the length scale of photothermal damage on neighboring cells.

We further analyzed the dynamic response of *HSP70* mRNA induced photothermally (Figure 5 and Figures S9 and S10). With a short duration of irradiation (*e.g.*, 1−2 min), the cells near the laser exhibited only a small elevation of *HSP70* mRNA expression. With longer irradiation durations, the *HSP70* expression for most cells within 100−400 μm increased asymptotically toward temperature-dependent steady-state values. Figure 5a−c shows the heat shock response between 40 and 44 °C. We excluded the data for the cells experiencing high temperature (>44 °C) due to the loss of *HSP70* expression. The data followed the

first-order kinetics, allowing the time constants and amplitudes to be extracted (Figure 5d). The time constant increased linearly with respect to the irradiation time, suggesting the cell actively responded to continuous irradiation (Figure 5e). Remarkably, the time constant was insensitive to temperature between 40 to 44 °C. In contrast, the amplitude of *HSP70* expression increased with both irradiation time and temperature in a nonlinear manner (Figure 5f). The cells near the laser responded to both amplitude and duration of laser irradiation dynamically, highlighting the complex cellular heat shock response and the importance of monitoring cellular responses during photothermal manipulation.

In this study, we demonstrate the multimodal GNR approach for photothermal operation and monitoring the spatiotemporal gene expression in living cells and tissues. The technique allows us to study the dynamic cellular response induced photothermally. In particular, heat shock triggers multiple signaling pathways and complex regulation of gene expression in cells and tissues.[38,39] Our *HSP70* mRNA and cell viability data illustrate the complex spatiotemporal dynamics in which the combined effects of irradiation duration and associated temperature elevation are critical during photothermal operation and should be considered for utilizing plasmonic nanostructures. This is particularly important in cases that require high laser power or long duration, such as cancer photothermal therapy, tissue ablation, physical manipulation of cells, and gene manipulation. Previous characterization of the photothermal response primarily relied on immunochemistry and RNA *in situ* hybridization in fixed cells and tissues. These techniques have limited abilities to measure the spatiotemporal gene expression profiles and to reveal the characteristics of the dynamic heat
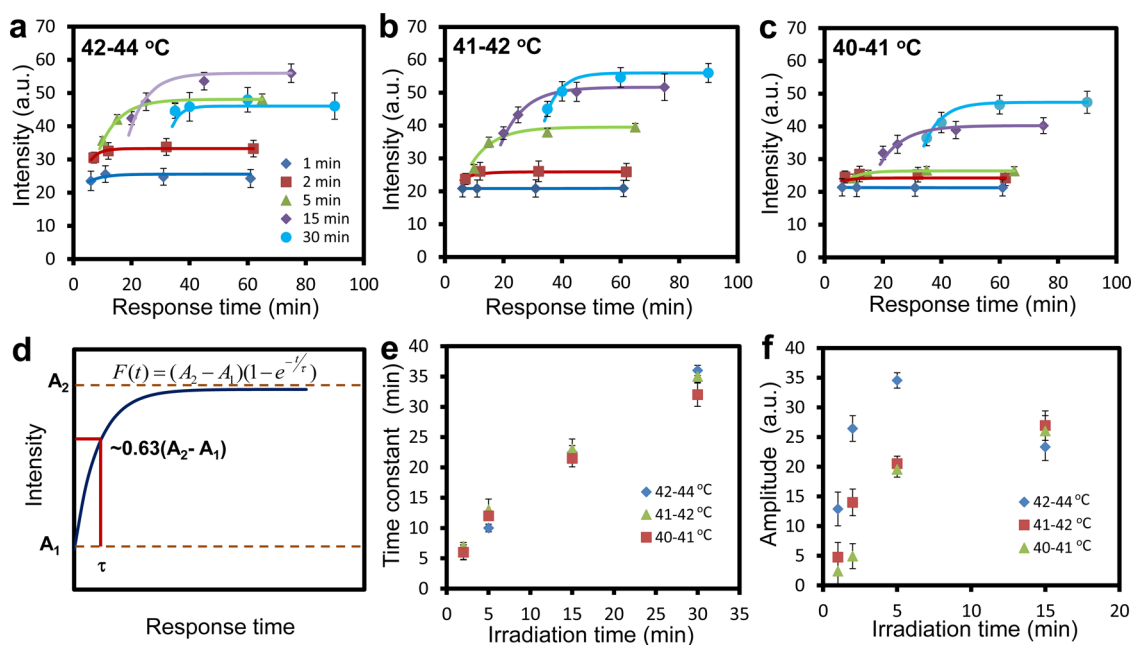
Figure 5. Dynamics of *HSP70* expression and regulation. (a−c) Dynamic intensity profiles of *HSP70* probes under different temperatures and irradiation durations. Lines are curve fitting using the equation defined in d. (d) Kinetic equation for estimating the time constant, τ, and amplitude, $A_2 - A_1$. (e,f) Time constants and amplitudes of *HSP70* expression extracted from data in a−c. Each data point is an average of at least 50 cells from three independent experiments. The data are expressed as mean ± SEM.

shock response. With its simplicity and effectiveness for mapping intracellular gene expression, the multimodal GNR−LNA is anticipated to serve as a platform technology for characterizing the cell behaviors during photothermal manipulations and optimizing the performance of plasmonic nanostructures toward a wide spectrum of biomedical applications in the future.

CONCLUSIONS

In summary, we demonstrate a GNR−LNA complex for monitoring intracellular gene expression in living cells and tissues. The gold nanorod quenches the fluorophore with high efficiency and allows intracellular delivery to living cells and tissues without the requirement of transfection reagents or microinjection. Furthermore, the complex enables us to monitor the dynamic gene expression of cells near the site of photothermal operation. The GNR−LNA represents a highly effective approach for intracellular gene expression analysis and has the potential for characterizing the photothermal effects of nanostructures in a wide spectrum of biomedical applications.

MATERIALS AND METHODS

Cell Culture. Human breast adenocarcinoma cells (MCF7) were obtained from American Type Culture Collection (ATCC HTB22). Cells were cultured in Dulbecco's modified Eagle medium (Invitrogen) supplemented with 10% deactivated fetal bovine serum (Gemini BioProducts), 2 mM HEPES buffer (Sigma Aldrich), and 0.1% gentamycin (GIBCO).

Mice Tissues. Female C57BL/6 mice were fed on laboratory food and tap water *ad libitum* in a regular 12 h dark/light cycle. Preparation of precision-cut lung slices (PCLS) was performed as previously described.[40] Six weeks old mice were anesthetized through IP injection of 240 mg/kg avertin (2-2-2 tribromoethanol, Sigma Aldrich). The skin was dissected from the abdomen to the neck, and the pleural cavity and trachea were exposed. The trachea was cannulated, and the animals were exsanguinated by cutting aortaventralis. Lungs were filled *in situ* with 38 °C 0.75% agarose (Research Products International Corp.) in minimal essential medium (MEM) and covered with ice for 10 min. Lungs were removed from the thoracic cavity into a plate filled with PBS and cooled on ice for an additional 10 min. Ten millimeter diameter tissue cores were prepared using a sharpened stainless steel tube. Lung tissue

cores were cut with a Brendel/Vitron Tissue Slicer (VITRON. Inc.) into 500−600 μm thin slices. Lung slices were incubated in MEM with 0.5% gentamycin at 37 °C, 5% CO$_2$, and 100% air humidity under cell culture conditions. Incubation medium was changed every 30 min for 2 h after slicing, and followed by a change every hour for the next 2 h, in order to remove agarose residues and cell debris from the tissue slices. To prepare precision-cut liver slices, the livers were placed into ice cold PBS for 10 min. Ten millimeter diameter tissue cores were prepared using a sharpened stainless steel tube. Liver tissue cores were then cut into thin slices (500−600 μm) and incubated in MEM with 0.5% gentamycin at 37 °C, 5% CO$_2$, and 100% air humidity for 90 min. The University of Arizona Institutional Animal Care and Use Committee approved all animal work and protocols.

Photothermal Ablation. Cell monolayers cultured on glass bottom culture dishes were incubated with different concentrations of GNRs, including 10^{10} GNR/mL, 2×10^{11} GNR/mL, and 5×10^{11} GNR/mL, for 12 h. Quantification of GNR internalized is described in supplementary section A. In the photothermal experiment, a 1064 nm fiber laser with stable high-quality TEM^{00} beam was utilized for laser irradiation. The laser module was attached to the microscope (Nikon, TE2000-U) through an epi-fluorescence port. To optimize the conditions, individual

cells were targeted at laser powers between 0 to 150 mW with a 40× objective, which focused the laser to 15 μm. For tissue studies, mice tissues were first incubated with 2×10^{11} GNR/mL for 12 h and then placed on glass bottom dish for single-cell ablation with irradiation intensity of 0.85 mW/μm^2.

Gene Expression Mapping. We designed probes for β-actin mRNA as a positive control and *HSP70* mRNA to study the cellular responses induced photothermally. A random probe sequence was also designed as the negative control to evaluate the selectivity of the assay. The specificity of the probe sequences has previously been tested and verified.[31] The cell monolayer and mice tissues were cultured in serum-free medium for 30 min before the GNR–LNA complexes were introduced with a concentration of 2×10^{11} GNR/mL for 12 h. To induce the photothermal effect, laser with 0.85 mW/μm^2 power density was irradiated to individual cells for durations of 1, 2, 5, 15, and 30 min. To determine the spatial gene expression profile near the laser, the fluorescence intensity of intracellular gene expression was measured at different locations. To measure the dynamic changes of gene expression, the intensity profiles of cells were monitored at different time points.

Imaging. Gene expression mapping with GNR–LNA complexes of living cells and tissues, and immunostaining experiments were performed using the inverted fluorescence microscope. Bright-field and fluorescence images were captured using an HQ2 CCD camera (Photometric, Tucson, AZ). For fluorescence microscopy, all images were taken with the same exposure time and conditions for comparing the intensity. To characterize GNR internalization, dark-field images were recorded by observing scattered light using a Nikon dark-field condenser (dry, 0.95–0.80 NA) coupled with the microscope. Data collection and imaging analysis were performed using the NIH ImageJ software.

Conflict of Interest: The authors declare no competing financial interest.

REFERENCES AND NOTES

1. Jung, H. S.; Kong, W. H.; Sung, D. K.; Lee, M. Y.; Beack, S. E.; Keum, D. H.; Kim, K. S.; Yun, S. H.; Hahn, S. K. Nanographene Oxide–Hyaluronic Acid Conjugate for Photothermal Ablation Therapy of Skin Cancer. *ACS Nano* **2014**, *8*, 260–268.

2. Kim, J. W.; Galanzha, E. I.; Shashkov, E. V.; Moon, H. M.; Zharov, V. P. Golden Carbon Nanotubes as Multimodal Photoacoustic and Photothermal High-Contrast Molecular Agents. *Nat. Nanotechnol.* **2009**, *4*, 688–694.

3. Jang, B.; Park, J. Y.; Tung, C. H.; Kim, I. H.; Choi, Y. Gold Nanorod–Photosensitizer Complex for Near-Infrared Fluorescence Imaging and Photodynamic/Photothermal Therapy *in Vivo*. *ACS Nano* **2011**, *5*, 1086–1094.

4. Huang, X.; El-Sayed, I. H.; Qian, W.; El-Sayed, M. A. Cancer Cell Imaging and Photothermal Therapy in the Near-Infrared Region by Using Gold Nanorods. *J. Am. Chem. Soc.* **2006**, *128*, 2115–2120.

5. Wu, T. H.; Teslaa, T.; Kalim, S.; French, C. T.; Moghadam, S.; Wall, R.; Miller, J. F.; Witte, O. N.; Teitell, M. A.; Chiou, P. Y. Photothermal Nanoblade for Large Cargo Delivery into Mammalian Cells. *Anal. Chem.* **2011**, *83*, 1321–1327.

6. Chen, C. C.; Lin, Y. P.; Wang, C. W.; Tzeng, H. C.; Wu, C. H.; Chen, Y. C.; Chen, C. P.; Chen, L. C.; Wu, Y. C. DNA–Gold Nanorod Conjugates for Remote Control of Localized Gene Expression by Near Infrared Irradiation. *J. Am. Chem. Soc.* **2006**, *128*, 3709–3715.

7. Lee, S. E.; Sasaki, D. Y.; Park, Y.; Xu, R.; Brennan, J. S.; Bissell, M. J.; Lee, L. P. Photonic Gene Circuits by Optically Addressable siRNA–Au Nanoantennas. *ACS Nano* **2012**, *6*, 7770–7780.

8. Miao, X. Y.; Wilson, B. K.; Pun, S. H.; Lin, L. Y. Optical Manipulation of Micron/Submicron Sized Particles and Biomolecules through Plasmonics. *Opt. Express* **2008**, *16*, 13517–13525.

9. Suzuki, M.; Toyoda, N.; Shimojou, M.; Takagi, S. Infrared Laser-Induced Gene Expression in Targeted Single Cells of Caenorhabditis Elegans. *Dev. Growth Differ.* **2013**, *55*, 454–461.

10. Wilson, B. K.; Mentele, T.; Bachar, S.; Knouf, E.; Bendoraite, A.; Tewari, M.; Pun, S. H.; Lin, L. Y. Nanostructure-Enhanced Laser Tweezers for EfficientTtrapping and Alignment of Particles. *Opt. Express* **2010**, *18*, 16005–16013.

11. Chen, X.; Chen, Y.; Yan, M.; Qiu, M. Nanosecond Photothermal Effects in Plasmonic Nanostructures. *ACS Nano* **2012**, *6*, 2550–2557.

12. Farokhzad, O. C.; Langer, R. Impact of Nanotechnology on Drug Delivery. *ACS Nano* **2009**, *3*, 16–20.

13. Ferrari, M. Cancer Nanotechnology: Opportunities and Challenges. *Nat. Rev. Cancer* **2005**, *5*, 161–171.

14. Chow, E. K.; Ho, D. Cancer Nanomedicine: from Drug Delivery to Imaging. *Sci. Transl. Med.* **2013**, *5*, 216rv4.

15. Fang, J.; Chen, Y. C. Nanomaterials for Photohyperthermia: A Review. *Curr. Pharm. Des.* **2013**, *19*, 6622–6634.

16. Anikeeva, P.; Deisseroth, K. Photothermal Genetic Engineering. *ACS Nano* **2012**, *6*, 7548–7552.

17. Wu, T. H.; Teslaa, T.; Teitell, M. A.; Chiou, P. Y. Photothermal Nanoblade for Patterned Cell Membrane Cutting. *Opt. Express* **2010**, *18*, 23153–23160.

18. Coppens, Z. J.; Li, W.; Walker, D. G.; Valentine, J. G. Probing and Controlling Photothermal Heat Generation in Plasmonic Nanostructures. *Nano Lett.* **2013**, *13*, 1023–1028.

19. Madersbacher, S.; Grobl, M.; Kramer, G.; Dirnhofer, S.; Steiner, G. E.; Marberger, M. Regulation of Heat Shock Protein 27 Expression of Prostatic Cells in Response to Heat Treatment. *Prostate* **1998**, *37*, 174–181.

20. Gibbons, N. B.; Watson, R. W.; Coffey, R. N.; Brady, H. P.; Fitzpatrick, J. M. Heat-Shock Proteins Inhibit Induction of Prostate Cancer Cell Apoptosis. *Prostate* **2000**, *45*, 58–65.

21. Soti, C.; Nagy, E.; Giricz, Z.; Vigh, L.; Csermely, P.; Ferdinandy, P. Heat Shock Proteins as Emerging Therapeutic Targets. *Br. J. Pharmacol.* **2005**, *146*, 769–780.

22. Ciocca, D. R.; Clark, G. M.; Tandon, A. K.; Fuqua, S. A. W.; Welch, W. J.; Mcguire, W. L. Heat-Shock Protein-Hsp70 in Patients with Axillary Lymph Node-Negative Breast-Cancer— Prognostic Implications. *J. Natl. Cancer Inst.* **1993**, *85*, 570–574.

23. Fan, C. H.; Wang, S.; Hong, J. W.; Bazan, G. C.; Plaxco, K. W.; Heeger, A. J. Beyond Superquenching: Hyper-Efficient Energy Transfer from Conjugated Polymers to Gold Nanoparticles. *Proc. Natl. Acad. Sci. U.S.A.* **2003**, *100*, 6297–6301.

24. Dubertret, B.; Calame, M.; Libchaber, A. J. Single-Mismatch Detection Using Gold-Quenched Fluorescent Oligonucleotides. *Nat. Biotechnol.* **2001**, *19*, 365–370.

25. Seferos, D. S.; Giljohann, D. A.; Hill, H. D.; Prigodich, A. E.; Mirkin, C. A. Nano-Flares: Probes for Transfection and mRNA Detection in Living Cells. *J. Am. Chem. Soc.* **2007**, *129*, 15477–15479.

26. Cho, H.; Yeh, E. C.; Sinha, R.; Laurence, T. A.; Bearinger, J. P.; Lee, L. P. Single-Step Nanoplasmonic VEGF165 Aptasensor for Early Cancer Diagnosis. *ACS Nano* **2012**, *6*, 7607–7614.

27. Prigodich, A. E.; Randeria, P. S.; Briley, W. E.; Kim, N. J.; Daniel, W. L.; Giljohann, D. A.; Mirkin, C. A. Multiplexed Nanoflares: mRNA Detection in Live Cells. *Anal. Chem.* **2012**, *84*, 2062–2066.

28. Maxwell, D. J.; Taylor, J. R.; Nie, S. M. Self-Assembled Nanoparticle Probes for Recognition and Detection of Biomolecules. *J. Am. Chem. Soc.* **2002**, *124*, 9606–9612.

29. Campbell, M. A.; Wengel, J. Locked *vs.* Unlocked Nucleic Acids (LNA *vs.* UNA): Contrasting Structures Work towards Common Therapeutic Goals. *Chem. Soc. Rev.* **2011**, *40*, 5680–5689.

30. Wu, Y. R.; Yang, C. J.; Moroz, L. L.; Tan, W. H. Nucleic Acid Beacons for Long-Term Real-Time Intracellular Monitoring. *Anal. Chem.* **2008**, *80*, 3025–3028.

31. Riahi, R.; Dean, Z.; Wu, T. H.; Teitell, M. A.; Chiou, P. Y.; Zhang, D. D.; Wong, P. K. Detection of mRNA in Living Cells by Double-Stranded Locked Nucleic Acid Probes. *Analyst* **2013**, *138*, 4777–4785.

32. Riahi, R.; Long, M.; Yang, Y.; Dean, Z.; Zhang, D. D.; Slepian, M. J.; Wong, P. K. Single Cell Gene Expression Analysis in Injury-Induced Collective Cell Migration. *Integr. Biol.* **2013**, *6*, 192–202.

33. Link, S.; El-Sayed, M. A. Spectral Properties and Relaxation Dynamics of Surface Plasmon Electronic Oscillations in Gold and Silver Nanodots and Nanorods. *J. Phys. Chem. B* **1999**, *103*, 8410–8426.

34. Alkilany, A. M.; Nagaria, P. K.; Hexel, C. R.; Shaw, T. J.; Murphy, C. J.; Wyatt, M. D. Cellular Uptake and Cytotoxicity of Gold Nanorods: Molecular Origin of Cytotoxicity and Surface Effects. *Small* **2009**, *5*, 701–708.

35. Chithrani, B. D.; Ghazani, A. A.; Chan, W. C. W. Determining the Size and Shape Dependence of Gold Nanoparticle Uptake into Mammalian Cells. *Nano Lett.* **2006**, *6*, 662–668.

36. Rosi, N. L.; Mirkin, C. A. Nanostructures in Biodiagnostics. *Chem. Rev.* **2005**, *105*, 1547–1562.

37. Connor, E. E.; Mwamuka, J.; Gole, A.; Murphy, C. J.; Wyatt, M. D. Gold Nanoparticles are Taken up by Human Cells but Do Not Cause Acute Cytotoxicity. *Small* **2005**, *1*, 325–327.

38. Kamei, Y.; Suzuki, M.; Watanabe, K.; Fujimori, K.; Kawasaki, T.; Deguchi, T.; Yoneda, Y.; Todo, T.; Takagi, S.; Funatsu, T.; Yuba, S. Infrared Laser-Mediated Gene Induction in Targeted Single Cells *in Vivo*. *Nat. Methods* **2009**, *6*, 79–81.

39. Shamovsky, I.; Ivannikov, M.; Kandel, E. S.; Gershon, D.; Nudler, E. RNA-Mediated Response to Heat Shock in Mammalian Cells. *Nature* **2006**, *440*, 556–560.

40. Henjakovic, M.; Martin, C.; Hoymann, H. G.; Sewald, K.; Ressmeyer, A. R.; Dassow, C.; Pohlmann, G.; Krug, N.; Uhlig, S.; Braun, A. *Ex Vivo* Lung Function Measurements in Precision-Cut Lung Slices (PCLS) from Chemical Allergen-Sensitized Mice Represent a Suitable Alternative to *In Vivo* Studies. *Toxicol. Sci.* **2008**, *106*, 444–453.

Supplementary Information

Mapping Photothermally Induced Gene Expression in Living Cells and Tissues by Nanorod-Locked Nucleic Acid Complexes

Reza Riahi[a], Shue Wang[a], Min Long [b,c], Na Li[d], Pei-Yu Chiou[e], Donna D. Zhang[b], Pak Kin Wong[a*]

[a]Department of Aerospace and Mechanical Engineering, University of Arizona, Tucson, AZ 85721 USA

[b]Department of Pharmacology and Toxicology, University of Arizona, Tucson, AZ 85724, USA.

[c]Department of Endocrinology, Xinqiao Hospital, Third Military Medical University, Chongqing 400037, PR China

[d]Department of Mechanical and Aerospace Engineering, University of Miami, Coral Gables, FL 33146, USA

[e]Department of Mechanical and Aerospace Engineering, University of California, Los Angeles, CA 90095, USA

*Corresponding author: Pak Kin Wong. Phone: 520-626-2215. E-mail: pak@email.arizona.edu

A. Experimental methods

B. Numerical analysis of temperature profiles

C. Supplementary tables

D. Supplementary figures

E. Supplementary movies

F. Reference

A.   Experimental methods

LNA probe design

All LNA probes were synthesized by Integrated DNA Technologies (IDT). The single-stranded locked nucleic acid (LNA) probe consists of alternating LNA/DNA monomers and is complementary to the target nucleic acid sequence. The alternating LNA/DNA is previously shown to optimize the binding affinity and the stability of the probes, resulting in enhanced performance for intracellular measurement.[1-4] The LNA probe is labeled with a fluorophore (6-FAM) located at the 5' end. In the present study, LNA probes and corresponding target DNA were synthesized by Integrated DNA Technologies Inc. The target gene sequences were obtained from the NCBI GenBank database (Supplementary Table S1). A random probe with no known complementary sequence in the human genome was designed as the negative control. All sequences were analyzed by NCBI Basic Local Alignment Search Tool database to evaluate the specificity. The Mfold web server was utilized to estimate the probe-target binding dynamics and secondary structures.[5] The gold nanorod-locked nucleic acid (GNR-LNA) complexes were used for real-time monitoring of specific target mRNA in living cells and tissues. Intracellular gene expression analysis was achieved by taking advantage of the intrinsic fluorescence quenching property of gold nanoparticles.[6] In the absence of a target mRNA, the fluorescently labeled LNA is quenched due to proximity with the GNR surface. However, upon hybridization to target RNA the probe is separated from the GNR and releases into the cytoplasm. This event allows fluorescence emission of the LNA probe with the presence of the target mRNA. To evaluate the quenching efficiency

of GNR, the double-stranded LNA probe[3] was used for comparison (Supplementary Fig. S2).

Characterization and preparation of the GNR-LNA complexes

GNRs with 10 nm in width and 67 nm in length were purchased from Nanopartz with mercaptoundecyltrimethylammonnium bromide (MUTAB) as a surfactant. These GNRs were synthesized according to the seed-mediated growth method resulted with high yield and monodispersity that allows a narrow plasmon resonance band.[7] In the calibration experiments with synthetic targets, 5×10^{11} GNR/ml was prepared to allow at least 1.2 μm interparticle separation avoiding interparticle coupling between the plasmon-enhanced electric filed.[8] Then, 30 nM LNA probe was introduced to the GNR solution to fully saturate the GNRs surface based on electrostatic interaction between the GNR and LNA probes while maintaining minimum background noise. The GNR-LNA complexes were allowed to equilibrate for 30 min at room temperature before mixing with the target solution (500 nM) for detection (Supplementary Fig. S2).

Quantification of LNA bound on the GNR surface

The LNA probe spontaneously binds to the GNR due to the interaction between nucleic acids and gold nanoparticles. To quantify the amount of LNA probe attached to a nanorod, mercaptoethanol was used to displace the LNA probe.[9] After displacement, the sample was centrifuged and supernatant containing the LNA probe was isolated from the GNR for fluorescence characterization. The fluorescence intensity of the sample was measured and the amount of LNA probes displacement was quantified.

Dividing the number of GNRs determined by UV-Vis extinction measurement yield the number of LNA probe attached to a single GNR to approximately 34 LNA per GNR. Considering each GNR carries ~34 copies of LNA probes in a cell, the final probe concentration inside a cell was approximately 45 nM. For cell imaging, 2×10^{11} GNR/ml GNR-LNA complexes targeting *heat shock protein 70* (*HPS70*) mRNA, β-actin mRNA, and random sequence were tested.

Quantification of internalized GNRs

Inductively coupled plasma mass spectrometry (ICP-MS) was applied to quantify GNRs internalizations. Briefly cells were cultured overnight. GNRs with concentration of 10^{10}, 2×10^{11}, and 5×10^{11} GNR/ml were introduced to 24 well plates and incubated for 12 hours. Cells were then washed for 3 times with 1X PBS to remove excessive GNRs that were not internalized. Cells were harvested with 0.25% trypsin solution and centrifuged at 1500 rpm for 5 min. The cell pellets were then resuspended in 1X PBS to obtain a final concentration of 5×10^5 cell/ml. The GNR samples were prepared by acid digestion of cells using the CEM MARS6 microwave digestion system (Matthews, N.C.). The sample was weighed in a tared Teflon vessel. Freshly-prepared aqua regia (Aristar-Plus grade HNO3:HCl at 1:3 ratio) was added. After one hour of pre-digestion, 1.0 ml of 18 megohm water was added prior to sealing the vessels. During the digestion process, the temperature of the solution reached to $200^{o}C$ after 20 min, and was held at this temperature for an additional 15 min. After cooling, the digest was transferred into a pre-weighed 15mL trace-metal-free PP tube (VWR Scientific). The mass of GNRs in the solution were then determined by Agilent 7700x CIP-MS system

(Agilent Technologies, Santa Clara, CA) and converted to the number of GNRs per cell using the calculated number of gold atom in each nanorods according to the equation previously reported[10].

Statistical analysis.

All experiments were performed independently for at least three times. For mapping the spatial and temporal heat shock response of cells after laser irradiation, at least 50 cells were measured for each data point. The data are expressed as mean ± SEM. For characterizing laser induced temperature elevation, the experiments were repeated (n=3) for statistical analysis. Statistical analysis was carried out using Student's t-test.

Temperature measurement

The temperature was measured at different time points and locations from the laser. For thermal heating and cooling experiments, miniaturized thermocouples (Omega) with 10 μm diameter were placed inside the media near the cell monolayer. Data were recorded using a thermocouple reader (Okolab) at different time points. The thermocouple was placed at different locations using a costumed 3D traversing system to determine the temperature distribution near the laser. To verify the temperature measurement and resolve the spatial temperature distribution, infrared thermometry was also performed using a mid-wavelength infrared camera (SC6700, FLIR Thermovision). The camera was positioned on top of the microscope stage to monitor the temperature distribution. Thermal analysis software (FLIR ExaminIR V.2.0) was used for data acquisition and analysis. To determine the heating and cooling time constants, the temperature profiles were measured after applying and terminating the

laser with 150 mW (a power density of 0.85 mW/μm^2). This setting was also used in the heat shock response mapping experiments. Numerical analyses were performed using the theory described in Supplementary Section B to compare with the experimental measurement.

B. Numerical analysis of temperature profile

Heat equation

To investigate the temperature distribution near the site of photothermal operation and the effects of laser power and duration, we performed computational analyses to estimate the temperature profile near the irradiation area. In particular, the heat diffusion equation, which describes the distribution of temperature over time, was considered in the analysis[11]. A heating term was introduced to represent the localized heat generated due to the photothermal effect (equation S1).

$$\frac{\partial T}{\partial t} = D\nabla^2 T + S \tag{S1}$$

where T is the temperature distribution and S is the local photothermal heating source. D is the thermal diffusivity of the medium. Thermal diffusivity of water was used in the calculation. The value can be modified to describe the heat transfer in other media. The localized heating is modeled by assigning an appropriate temperature at the location of photothermal operation. The partial differential equation was written in two-dimensional form to approximate the photothermal ablation experiment (equation S2). The equation was discretized in space and time using the finite difference approach and implemented in MATLAB (equation S3).[12] n, i, and j are discrete time and space indexes.

$$\frac{\partial T}{\partial t} = D\left(\frac{\partial^2 T}{\partial x^2} + \frac{\partial^2 T}{\partial y^2}\right) + S \tag{S2}$$

$$T_{i,j}^{n+1} = T_{i,j}^n + D\left(\frac{T_{i+1,j}^n - 2T_{i,j}^n + T_{i-1,j}^n}{(\Delta x)^2} + \frac{T_{i,j+1}^n - 2T_{i,j}^n + T_{i,j-1}^n}{(\Delta y)^2}\right)\Delta t + S\,\Delta t \tag{S3}$$

Boundary and initial conditions

Supplementary Fig. S4a shows the domain considered in the simulation. In the simulation domain, there were 20 by 80 elements and each element was 100 μm by 100 μm in size. Initial and boundary conditions were required to solve the heat equation. For initial condition, the temperature was considered to be uniform at the reference temperature initially. The thermal boundary condition was determined by the heat transfer through the cover slip (Supplementary Fig. S4b). In particular, the heat loss to the cover glass was determined by the heat transfer coefficients at the liquid-glass interface and glass-air interface, and conductive heat transfer through the cover glass. T_f, T_s, T_b, and T_∞ were the temperature of the liquid, the liquid-glass interface, the glass-air interface, and the ambient. In our experimental condition, the heat flux was mainly determined by the heat transfer coefficient at the glass-air interface. Since most of the heat loss occurred near the laser source on the cover glass, the heat transfer was considered to be the same in all boundaries. The parameters and values used in the numerical simulation are described in Table S2.[11]

Temperature distribution with continuous laser irradiation

The temperature profiles with continuous laser heating were shown in Fig. 2h in the main text (see also Supplementary movie S3). In the simulation, heat diffused rapidly to the surrounding media in the first few seconds. The temperature profile then gradually reached a quasi-steady state value when the heat flux is approximately equal to the heat loss to the substrate. Supplementary Fig. S5 shows the temperature profiles near the laser. The region of temperature elevation was localized near the heat source. The temperature dropped to 50% of the maximum value in 200-300 μm, representing a characteristic heat transfer length scale of the system. This length scale was in good agreement with the value measured in the experiment by infrared thermometry and miniaturized thermocouples (see Fig. 2e).

Heating and cooling time constants

To estimate the thermal time constants of the system, numerical simulation of heating and cooling experiments were performed. The temperature distributions at several locations away from the laser source are shown in Fig. S6. At a location near the laser (*e.g.*, less than 100 μm), the temperature rapidly reached a high value in approximately 3 sec and increased gradually afterward (see also Supplementary movie S3). Our observation suggested that two time scales were involved in the system. Examining the parameter space revealed that the two time scales were related to the convective heat transfer at the boundary and conductive heat transfer in the bulk solution. To investigate the cooling time constant, the heat source was removed after 10 sec of heating. Similarly, a rapid drop in the temperature was observed initially and followed by a slow decay of the temperature. These observations were in general agreement

with the experiment measurement, supporting the use of the numerical analysis for interpreting the temperature distribution near the site of photothermal operation.

Effects of laser duration

We then investigated the effects of the duration of heating on the temperature profile. Supplementary Fig. S7 shows the temperature distributions with different heating durations. In general, a short heating duration, relative to the heating time constant, will result in a localized heating effect, since the heating source was removed before the heat accumulate and propagate to a location away from the heating source. For instance, limiting the heating duration to 2 sec will significantly reduce the maximum heating compared to continuous irradiation. Supplementary movies S4-6 illustrated the spatiotemporal temperature distribution with different heating durations.

C. Supplementary Tables

Table S1. Sequences of single-stranded LNA probes with alternating DNA/LNA monomers for intracellular detection. Bold italic letters represent LNA monomers.

Target Gene	Name	Sequence/Label	Length (base)	ΔG_{DT} (kcal/mol)
β-actin	Donor (D)	5'-/FAM-6/*AGGA*AG*GA*AG*GCT*GG*A*A*GA*G/-3'	20	-25.8
	Quencher (Q)	5'-/*CT*TC*C*T*TC*CT/Iowa Black RQ/-3'	10	
	Target (T)	5'-/CTCTTCCAGCCTTCCTTCCT/-3'	20	
HSP70	Donor (D)	5'-/FAM-6/*TT*G*TC*G*TT*GG*T*GA*T*GG*T*GA*T/-3'	20	-24.9
	Target (T)	5'-/ATCACCATCACCAACGACAA/- 3'	20	
Random	Donor (D)	5'-/FAM-6/*ACGC*GA*CA*AG*CGCACC*GAT*A/-3'	20	-26.2
	Target (T)	5'/TATCGGTGCGCTTGTCGCGT/3'	20	

Table S2. Parameters in the numerical simulation.

Parameters	Symbols	Values	Units
Heat diffusivity of water	D	0.143×10^{-6}	m^2/s
Cover slip thickness	L	170×10^{-6}	m
Thermal conductivity	k	1.13	W/(mK)
Heat transfer coefficient, air	h_a	2.5	$W/(m^2K)$
Heat transfer coefficient, water	h_l	100	$W/(m^2K)$

D.   Supplementary figures
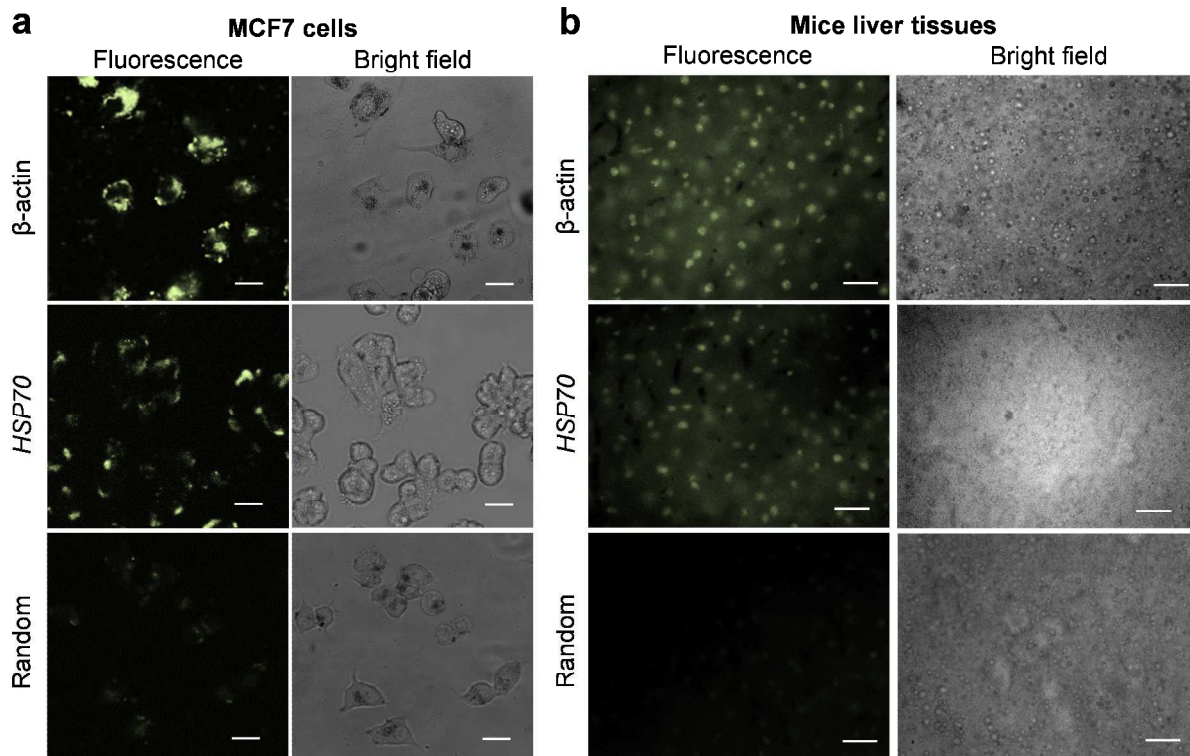
Figure S1. Intracellular gene expression analysis. a-b, Intracellular gene expression of β-actin and *HSP70* mRNAs in (a) MFC7 cells and (b) mice liver tissues. A random sequence is designed as the negative control. The intensity in the cytoplasm of each cell can be extracted from the images to map the spatiotemporal gene expression dynamics. Scale bars, 25 µm.
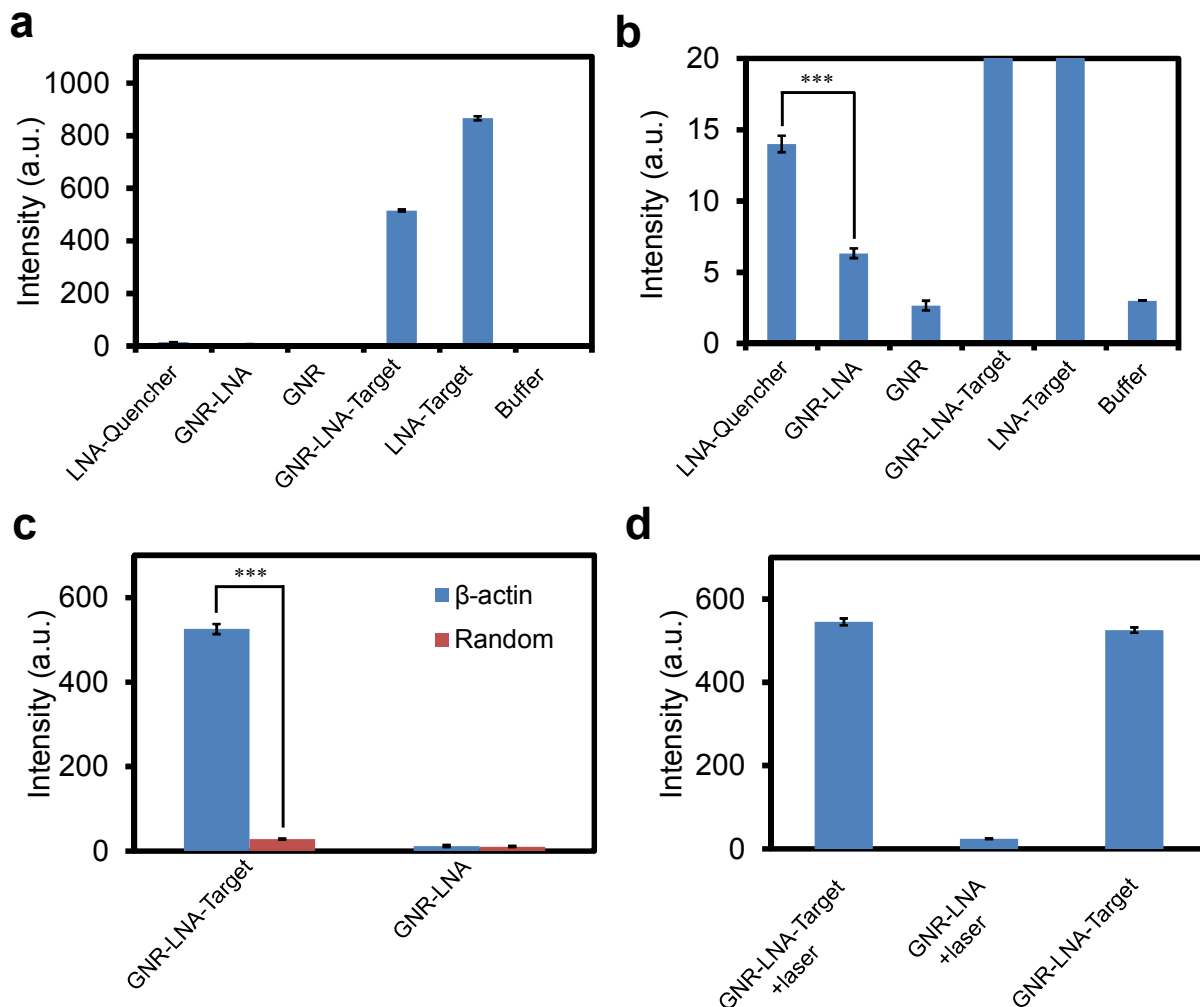
Figure S2. Characteristics of the GNR-LNA complexes for gene expression analysis. a, The quenching efficiency of GNR was compared to a complementary LNA sequence labeled with an organic quencher (quencher sequence). Iowa black was used as the organic quencher for comparison. The quencher sequence and the LNA probe were heated to 95°C for 5 min and cooled down slowly for hybridization. The GNR reduced the fluorescence signal for 137 folds compared to the probe hybridized to the target DNA (i.e., quenching efficiency ~99.27%). b, (a) is plotted in the low intensity range to illustrate the quenching efficiency of GNR compared to the organic quencher. The quenching efficiency of GNR is 2.4-fold better than the quencher

sequence.   c, Specificity of the GNR-LNA complexes.   A synthetic DNA sequence complementary to the β-actin probe was applied and the target concentration was 500 nM. The random probe was included to test the specificity of the assay. d, Laser irradiation to the GNR-LNA complexes with and without the complementary synthetic target sequence. The LNA probe concentration was 30 nM in all cases. Statistical analysis, n=3 (***, $P < 0.001$).
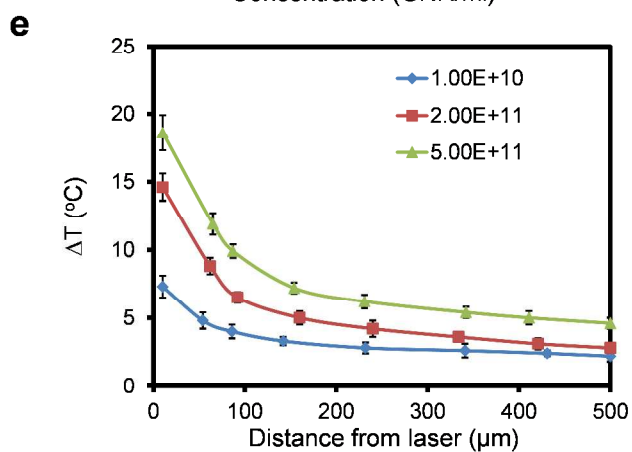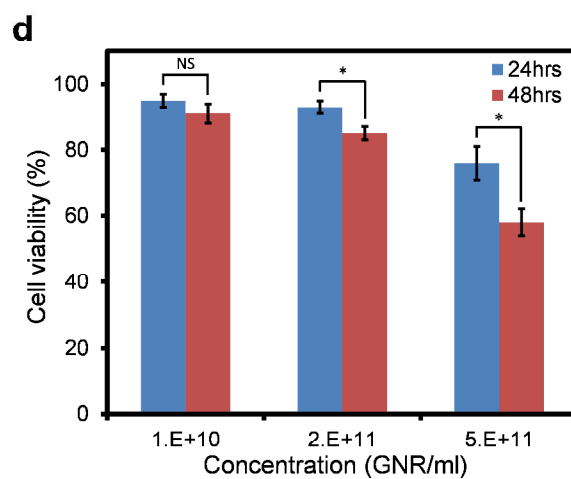
a

b GNRs | Control

c

d

e

f

g Without GNR
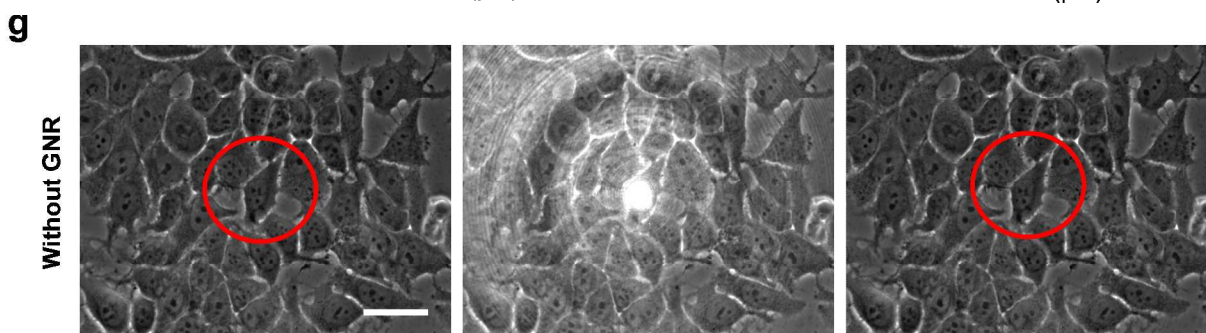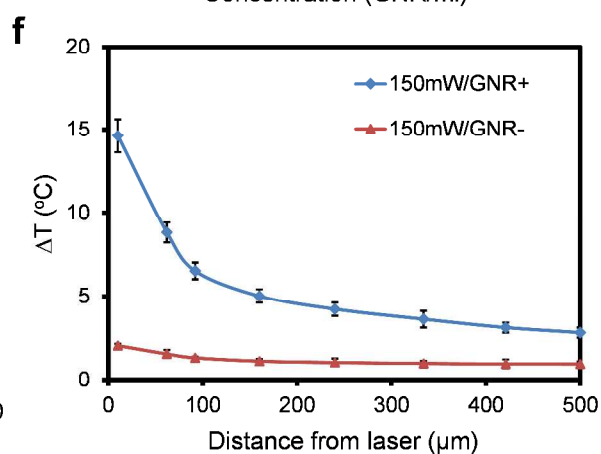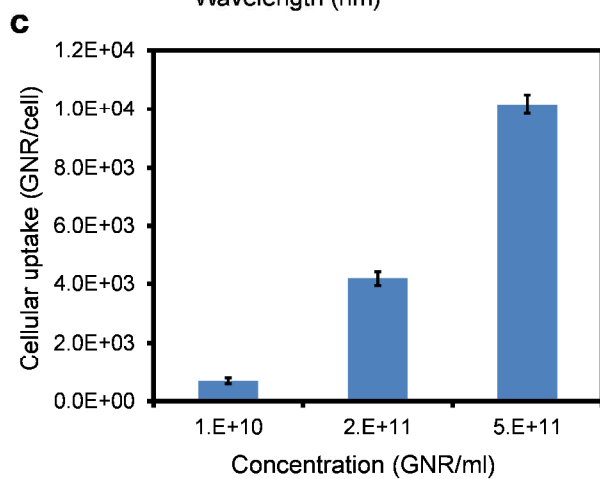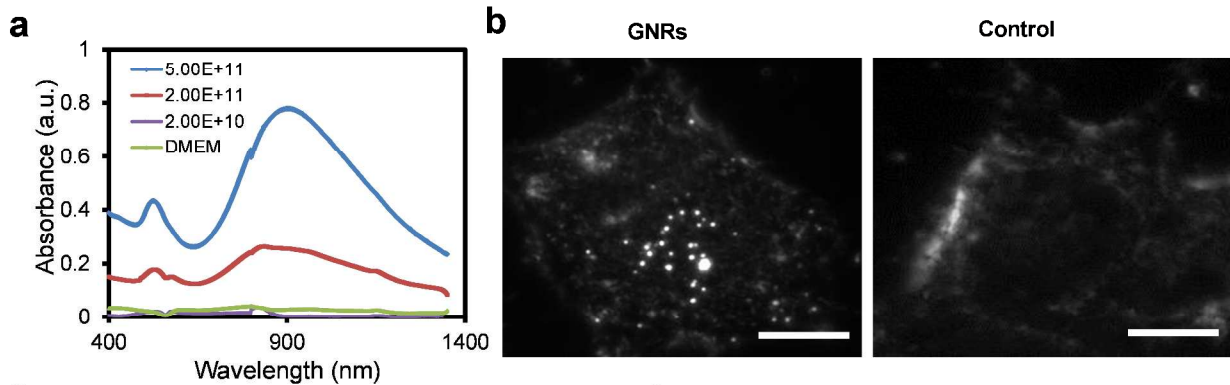
Figure S3. GNRs uptake and photothermal effect. a, UV-Vis spectroscopy for determining the absorption spectrum of the GNR in DMEM. b, Dark field microscopy for observing GNRs in living cells. Control represents a cell that was not incubated with GNR. c, The effect of GNR concentration during incubation on intracellular uptake of GNRs determined by ICP-MS. d, The effect of GNR concentration on cell viability. The measurements were done after 24 hr and 48 hr of incubation. e, The temperature distributions obtained with different concentrations of GNR and a laser power of 150 mW. f, Comparison of temperature distribution with and without internalized GNRs. The laser with 150 mW was focused to a spot size of 15 μm. g, A control photothermal ablation experiment without GNRs. Cycles indicate the target cell in the ablation experiments. Scale bars, 25 μm. Statistical analysis, n=3 (NS, not significant; *, P < 0.05).
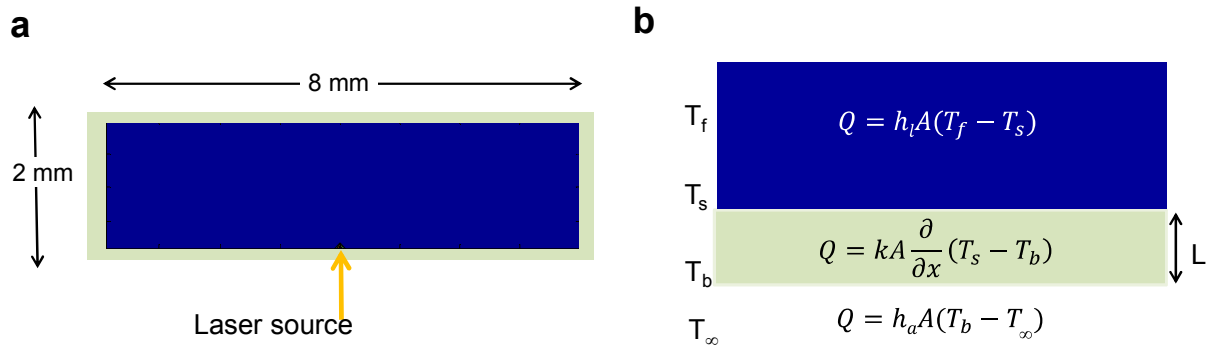
a

8 mm

2 mm

Laser source

b

T_f

$Q = h_l A(T_f - T_s)$

T_s

$Q = kA\dfrac{\partial}{\partial x}(T_s - T_b)$

T_b

L

T_∞

$Q = h_a A(T_b - T_\infty)$

Figure S4. Computational simulation of the temperature profiles. a, The domain considered in the numerical study. The arrow indicates the position of the localized heating source. b, Conductive and convective heat transfer near the glass cover slip for determining the thermal boundary condition.
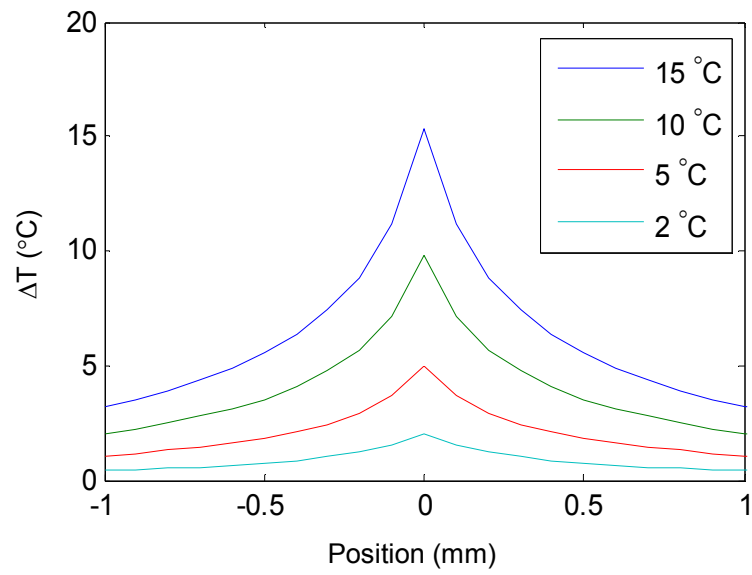
Figure S5. Temperature distribution. The local temperature profiles near the surface experienced by the cells. Different localized heating sources were applied at the origin.
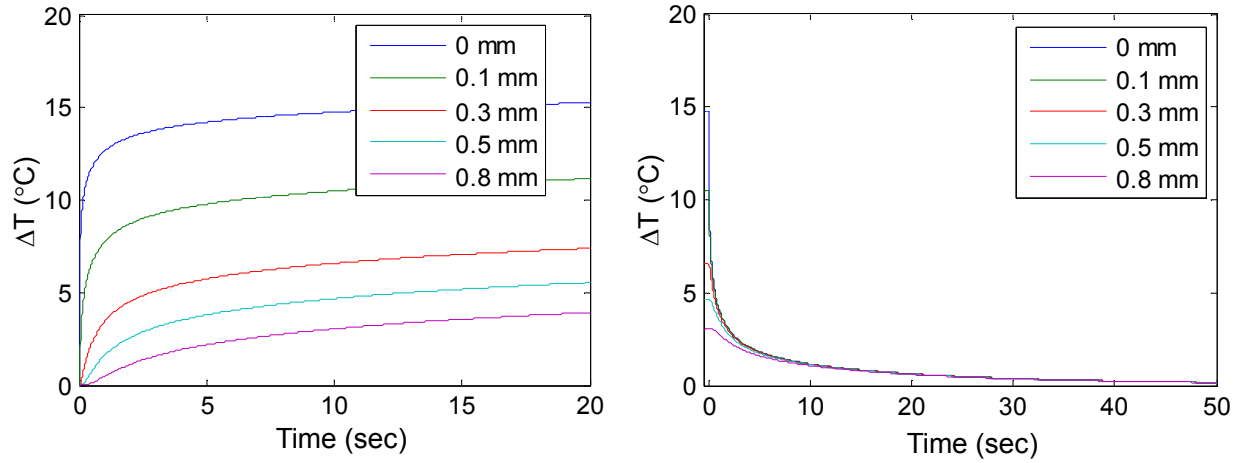
Figure S6. Thermal time constants. Thermal heating (left) and cooling (right) near the surface at different locations from the heating source.
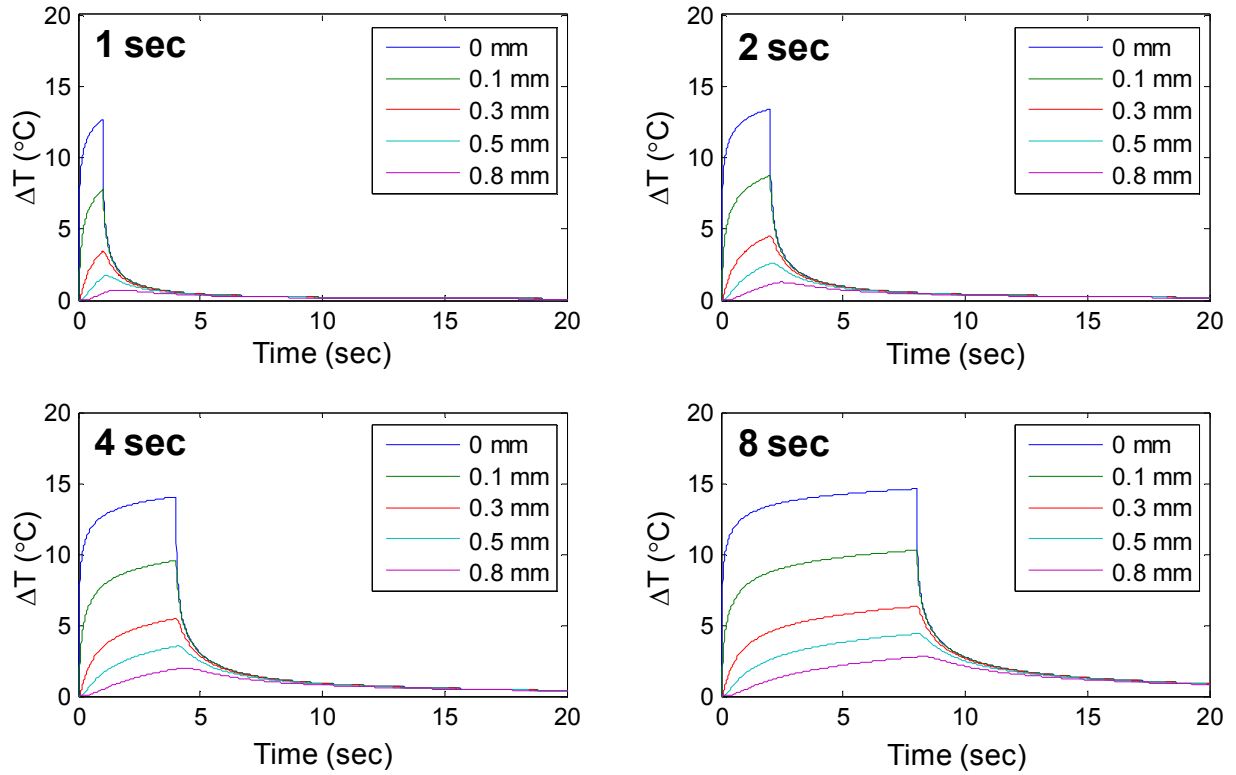
Figure S7. The effects of laser heating duration. The effects of laser duration on temperature profiles. The laser durations were 1, 2, 4, and 8 sec.
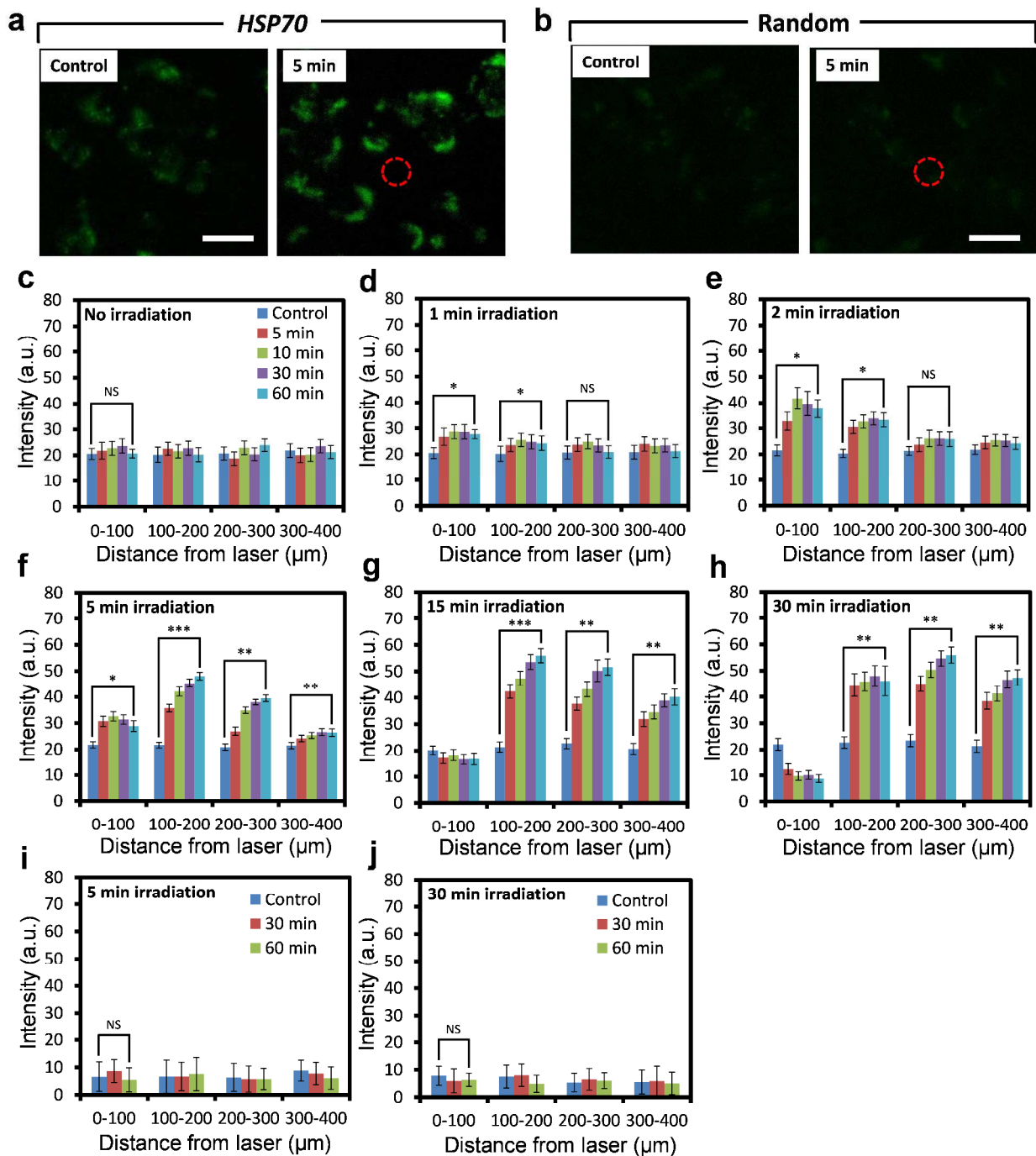
Figure S8. Mapping of *HSP70* gene expression distributions induced by laser irradiation of single cells. a-b, Fluorescence intensity observed before and after 5 min laser irradiation using GNR-LNA complexes. The LNA probes target *HSP70* mRNA and a random sequence. Red

circles indicate the locations of laser irradiation. Scale bar, 25 μm. c-h, Intercellular gene expression distribution in different locations. Laser was focused at the origin. The experiment was repeated with different durations of laser irradiation. A single cell was irradiated in each experiment. i-j, The intensity distributions of random probes with 5 min and 50 min of irradiation. Statistical analysis, n=3 (NS, not significant; *, P < 0.05; **, P < 0.01; ***, P < 0.001).
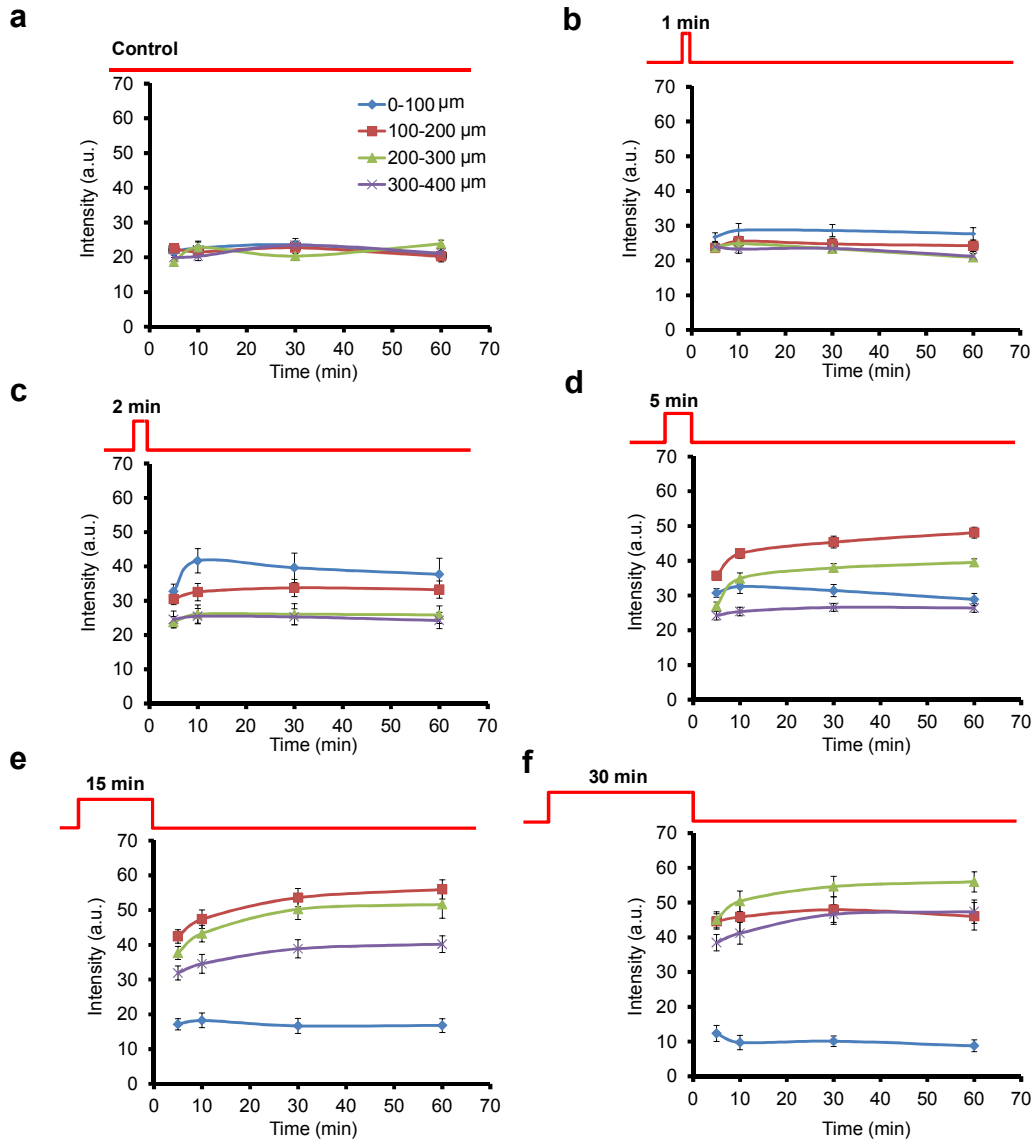

Figure S9. Dynamics of *HSP70* expression. a-f, Dynamics response of HSP70 mRNA after different durations of laser irradiation. Red lines indicate the time course of laser irradiation. Gene expressions were measured 5 min after termination of the laser.
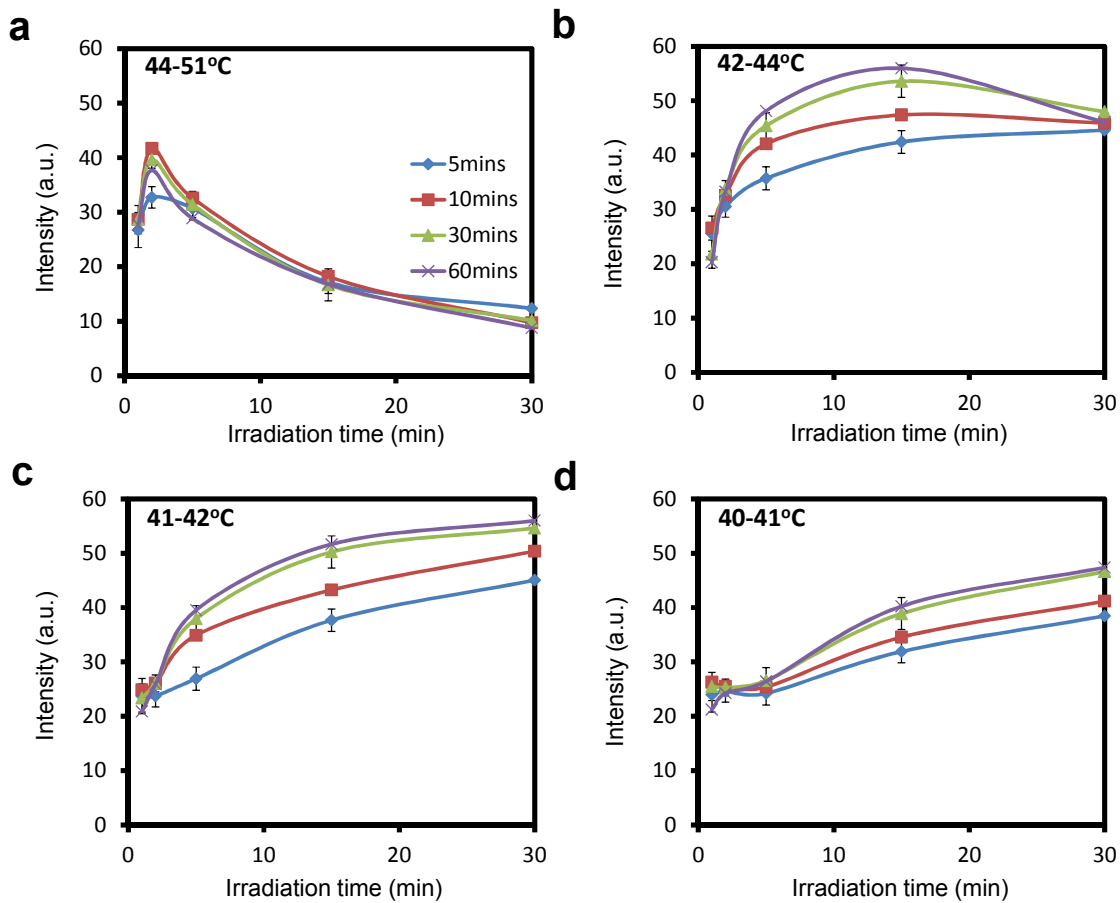
Figure S10. The effects of temperature on HSP70 expression kinetics. Dynamics response of HSP70 mRNA for cells experienced temperature from a, 44-51°C, b, 42-44°C, c, 41-42°C, and d, 40-41°C.

E. Supplementary Movies

Movie S1. A photothermal single cell ablation experiment. A single cell is irradiated by 150 mW laser power for 3 sec.

Movie S2. A control experiment of laser irradiation without GNRs. A single cell is irradiated with 150mW laser power for more than 7 sec.

Movie S3. Temperature distribution under continuous laser irradiation. The duration of simulation is 20 sec. The height and width of the simulation domain are 2 mm and 8 mm respectively.

Movie S4. Temperature distribution with 1 sec laser pulse. The duration of simulation is 10 sec.

Movie S5. Temperature distribution with 3 sec laser pulse. The duration of simulation is 10 sec.

Movie S6. Temperature distribution with 5 sec laser pulse. The duration of simulation is 10 sec.

F. Supplementary references

1.   Campbell, M. A.; Wengel, J. Locked vs. Unlocked Nucleic Acids (LNA vs. UNA): Contrasting Structures Work Towards Common Therapeutic Goals. *Chem. Soc. Rev.* 2011, 40, 5680-5689.

2.   Wu, Y. R.; Yang, C. J.; Moroz, L. L.; Tan, W. H. Nucleic Acid Beacons for Long-Term Real-Time Intracellular Monitoring. *Anal. Chem.* 2008, 80, 3025-3028.

3.   Riahi, R.; Dean, Z.; Wu, T. H.; Teitell, M. A.; Chiou, P. Y.; Zhang, D. D.; Wong, P. K. Detection of mRNA in Living Cells by Double-Stranded Locked Nucleic Acid Probes. *Analyst* 2013, 138, 4777-4785.

4.   Riahi, R.; Long, M.; Yang, Y.; Dean, Z.; Zhang, D. D.; Slepian, M. J.; Wong, P. K. Single Cell Gene Expression Analysis in Injury-Induced Collective Cell Migration. *Integr. Biol.* 2014.

5.   Zuker, M. Mfold Web Server for Nucleic Acid Folding and Hybridization Prediction. *Nucleic Acids Res.* 2003, 31, 3406-15.

6.   Dubertret, B.; Calame, M.; Libchaber, A. J. Single-Mismatch Detection using Gold-Quenched Fluorescent Oligonucleotides. *Nat. Biotechnol.* 2001, 19, 365-370.

7.   Sau, T. K.; Murphy, C. J. Seeded High Yield Synthesis of Short Au Nanorods in Aqueous Solution. *Langmuir* 2004, 20, 6414-6420.

8.   Huschka, R.; Zuloaga, J.; Knight, M. W.; Brown, L. V.; Nordlander, P.; Halas, N. J. Light-Induced Release of DNA from Gold Nanoparticles: Nanoshells and Nanorods. *J. Am. Chem. Soc.* 2011, 133, 12247-55.

9.   Maxwell, D. J.; Taylor, J. R.; Nie, S. M. Self-Assembled Nanoparticle Probes for Recognition and Detection of Biomolecules. *J. Am. Chem. Soc.* 2002, 124, 9606-9612.

10. Chithrani, B. D.; Ghazani, A. A.; Chan, W. C. W. Determining the Size and Shape Dependence of Gold Nanoparticle Uptake into Mammalian Cells. *Nano Lett.* 2006, 6, 662-668.

11. Das, S. K. *Fundamentals of Heat and Mass Transfer*. Alpha Science International: Oxford, U.K., 2010; p xvii, 826 p.

12. LeVeque, R. J. *Finite Difference Methods for Ordinary and Partial Differential Equations : Steady-State and Time-Dependent Problems*. Society for Industrial and Applied Mathematics: Philadelphia, PA, 2007; p xv, 341 p.